

MASSIVE QUIESCENT CORES IN ORION. IV. THEIR SUPERCRITICAL STATE REVEALED by HIGH RESOLUTION AMMONIA MAPS

D. Li^{1,2,3}, J. Kauffmann³, Q. Zhang⁴, W. Chen⁵

ABSTRACT

We present combined VLA and GBT images of NH_3 inversion transitions (1,1) and (2,2) toward OMC2 and OMC3. We focus on the relatively quiescent Orion cores, which are away from the Trapezium cluster and have no sign of massive protostars nor evolved star formation. The $5''$ angular resolution and 0.6 km s^{-1} velocity resolution of these data enable us to study the thermal and dynamic state of these cores at $\sim 0.02 \text{ pc}$ scales, comparable to or smaller than those of the current dust continuum surveys. We measure temperatures for a total of 30 cores, with average masses and radii of $11 M_\odot$ and 0.039 pc , respectively. Compared to other Gould Belt dense cores, more Orion cores have a high gravitational-to-kinetic energy ratio (virial mass ratio $R_{\text{vir}} > 3$), resembling results for other clouds forming high-mass stars. This results from Orion cores having velocity dispersions similar to those in, e.g., Perseus and Ophiuchus, but higher masses for given sizes. 12 out of 30 cores are associated with embedded YSOs identified by Spitzer. The protellar cores have a mean mass of $16.5 M_\odot$ versus $7.3 M_\odot$ for starless cores, while mean size and temperature are similar regardless of the cores' stellar content. 11 starless massive Orion cores are supercritical (mass-to-critical-mass ratio $R_c > 1$). These massive Orion starless cores will likely collapse or fragment quickly and can thus be considered direct precursors to protostars.

Subject headings: ISM:clouds – individual (Orion) – Stars:formation – instrumentation: interferometers

¹National Astronomical Observatories, Chinese Academy of Science, Chaoyang District Datun Rd A20, Beijing, China; *email:* ithaca.li@gmail.com

²Space Science Institute, Boulder, CO

³Jet Propulsion Laboratory, California Institute of Technology, Pasadena, CA, USA

⁴Harvard-Smithsonian Center for Astrophysics, Cambridge, MA, USA

⁵Peking University, Beijing, China

1. INTRODUCTION

Stars form in molecular clouds. Within molecular clouds, discrete structures with observable column density contrast, particularly in high density tracers, with its surroundings are referred to as cores (e.g. Benson & Myers 1989; Ward-Thompson et al. 2007). The relatively high extinction and density of cores make them the likely site for the onset of collapse.

Recent core surveys (e.g. Ikeda et al. 2007; Könyves et al. 2010; Sadavoy et al. 2010) are facilitated by focal plane imaging arrays of growing sizes. Although many surveys have large sample size in the hundreds, the majority of these studies are of dust continuum, which tend to focus on core mass function. Direct measurement of cores’ thermal and dynamic structures require spectra maps of high density tracers and preferably cover the same spatial dynamic ranges as those of the dust emission.

There seems to be an observational dichotomy between low mass star formation and high mass star formation. Massive stars are formed exclusively in giant molecular clouds and with higher efficiency. Due to the large distances of most massive star forming regions, many massive cores are under-resolved, showing signs of star formation well underway, such as H₂O masers (Mookerjee et al. 2004) and/or compact HII regions (Reid & Wilson 2005). At about 437 pc (Hirota et al. 2007; Menten et al. 2007), Orion molecular clouds are the closest massive star forming region with an OB cluster, thus particularly suited for studying the early stages of star formation in massive cores and/or under the influence of young massive stars. In a series of papers, we identified ‘quiescent’ Orion clouds/cores (containing no HII region, no IRAS point sources, and are at last 1 pc away from the OB cluster) with NH₃ and N₂H⁺ with a beam size of about 1′ (Li, Goldsmith & Menten 2003; hereafter paper I), presented high resolution 350 μ m images with a beam size of 9″ (Li et al. 2007; hereafter paper II), and revealed that two thirds of Orion cores have signatures of ongoing dynamic evolution, both outflows and inflows (Velusamy et al. 2008 hereafter paper III). Based on dust mass and dust core size (paper II), the majority of the cores are seemingly supercritical, i.e., no adequate support from thermal pressure, turbulence, or static magnetic field. This is consistent with the majority of the cores being hydrostatically unstable (paper III), which, however, could not be directly tested due to a lack of high resolution spectroscopic data.

Spectroscopic survey of CO 1-0 (Williams, Plambeck & Heyer 2003) and CO 3-2 (Takahashi et al. 2008) reveal that part of the Orion molecular cloud, namely, OMC2 and OMC3, contains many molecular outflows. OMC2 and OMC3 have also been mapped in high density tracers. Using the Nobeyama 45m telescope, Tatematsu et al. (2008) identified 34 cloud cores in N₂H⁺ 1-0 with a beam width of around 18″. Ikeda et al. (2007) studied dense gas in the same region using H¹³CO⁺ also with Nobeyama. These studies find higher column

density for respective tracers compared with low mass star forming regions, such as Taurus. NH_3 inversion transitions are particularly suited for studying dense cores due to their lack of depletion and their sensitivity to kinetic temperature (Ho & Townes 1983). Wiseman & Ho (1998) obtained NH_3 maps of a $8' \times 6'$ region around Orion-KL using VLA. The gas morphology there is dominated by quasi-parallel filaments severely influenced by the energy output of young massive stars.

In this letter, we present the combined VLA and GBT ammonia survey of the cores in OMC2 and OMC3. The spatial resolution of $\sim 5''$ and the spectral resolution of 0.6 km s^{-1} facilitate a detailed examination of the thermal and dynamic states of massive quiescent Orion cores.

2. OBSERVATIONS AND DATA REDUCTION

The VLA observations of OMC2/OMC3 were carried out in the D configuration on July 29 and September 24 of 2000. We used the correlator mode 4 to cover the NH_3 (J,K) = (1,1) and (2,2) inversion transitions simultaneously. With a primary beam of about $2'$ at the observing frequencies, a total of 20 pointings were used to mosaic the OMC2/3 regions. The correlator was configured to a bandwidth of 3.13 MHz for each transition that was divided into 64 channels, providing a velocity coverage of 40 km s^{-1} in 0.6 km s^{-1} channel spacing. We used quasar 3C286 as the flux calibrator and 3C84 or 3C273 as bandpass calibrators. The time dependent gains were monitored by observing 0539-057 or 0605-085. Visibility data were calibrated in AIPS and exported to MIRIAD for imaging. The 1σ RMS in the channel maps, after combining the two observations is about 8 mJy per spectral channel.

The observations of NH_3 (1,1) and (2,2) transitions with the GBT were taken on April 6th and 7th of 2005 in the OTF mode using the receiver Rcvr18-26. The correlator setup had a 200 MHz bandwidth and 0.31 km s^{-1} velocity resolution (8192 channels). The flat baseline and the wide bandwidth allowed us to use frequency switch with a throw of 12.5 MHz. The spectra were folded and the 3D data cube were resampled to a grid of $12''$ spacing and 0.3 km s^{-1} channel. The resulting GBT spectra has a typical 0.12 K RMS noise per channel.

We combine the NH_3 data from the VLA with those from the GBT to recover missing short spacing fluxes in the interferometric data. The combination was performed in the UV domain using MIRIAD, following the procedure outlined in Vogel et al. (1984) and Zhang et al. (2000). The NH_3 emission from the combined image, when convolved to the $30''$ GBT beam, recovers more than 80% of the fluxes detected in the GBT data. The integrated

intensity of the NH_3 (1,1) line with previously identified continuum sources and a pair of typical spectra are presented in Fig. 1.

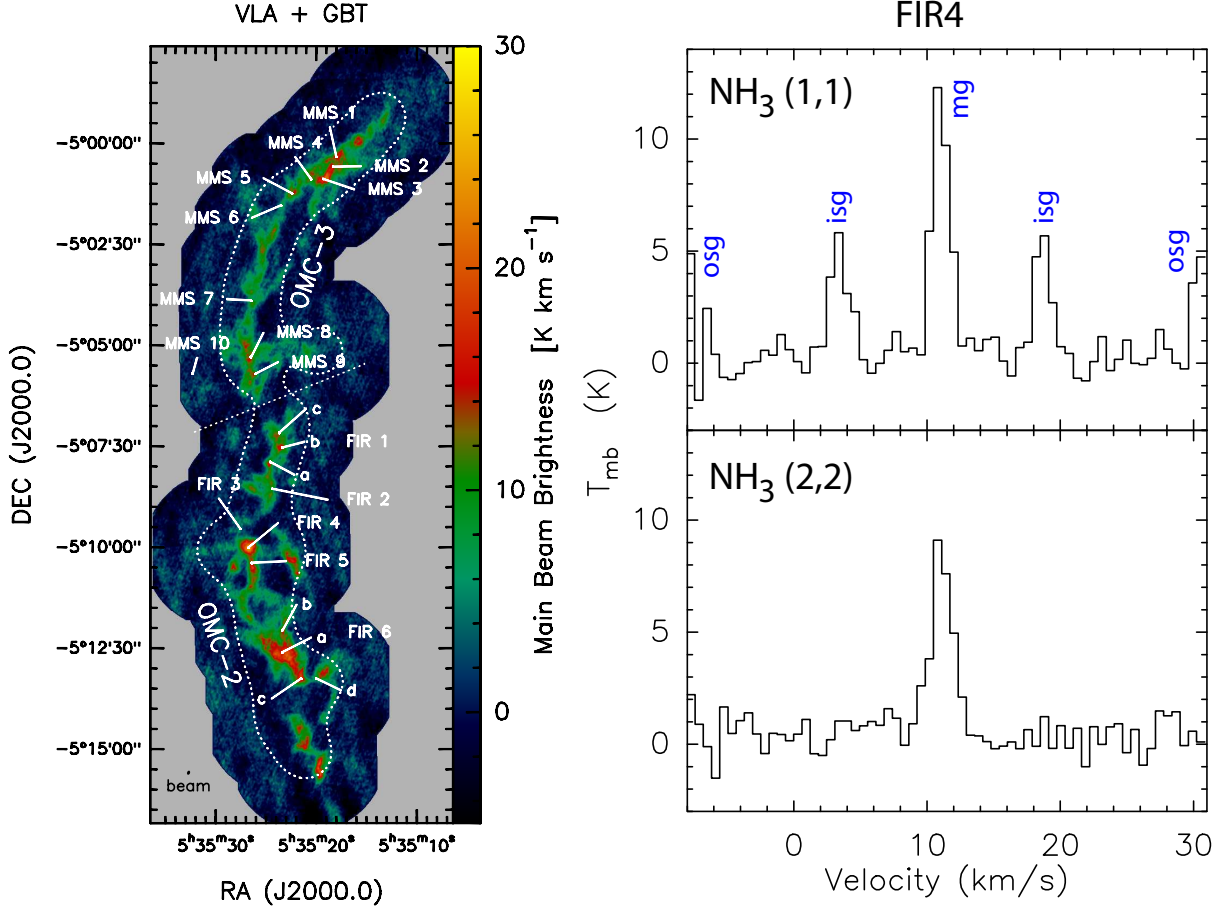


Fig. 1.— The integrated intensity of NH_3 (1,1) overlaid with dust continuum peaks from Chini et al. (1997) and references therein. The white dotted line indicates the location where the gain drops to 80% of the peak value. The spectra shown on the right are for the FIR 4 position, the brightest NH_3 peak in OMC 2. The VLA bandwidth covers fully the main group (mg) and the inner satellite groups (isg) of the hyperfine components, and only partially the outer satellite groups (osg).

3. Derivation of Kinetic Temperature and Velocity Dispersion

Largely following Ho & Townes (1983), Paper I described a recipe for deriving kinetic temperature from spectrally resolved, modestly blended NH_3 lines (intrinsic line width $\Delta V \sim$

1.0 km s^{-1}). In this paper, we report line width ΔV in FWHM. The one dimensional velocity dispersion σ used in Eq. 8, Eq. 11 and Eq. 12 is related to FWHM as $\Delta V = \sqrt{8 \ln(2)} \sigma$ for a Gaussian. The key step is to obtain the optical depth of the (1,1) line from simultaneously fitting all hyperfine components. As can be seen in Fig. 1, the VLA band is not wide enough to fully cover the two outer groups (*osg*). The combined data set thus only have the main and inner satellite components of the (1,1) transition and have a velocity resolution of 0.6 km s^{-1} . Toward most positions, the intrinsic line width is smaller or approaching channel width. For such under-resolved line, the opacity cannot be easily uniquely fitted.

We developed a more straightforward recipe utilizing two ratios between integrated intensities, which are directly observable, $\mathcal{R}^{12} = [\int T_A^{(mg+isg)}(1,1)d\nu]/[\int T_A(2,2)d\nu]$ and $\mathcal{R}^{sm} = [\int T_A^{(isg)}(1,1)d\nu]/[\int T_A^{(mg)}(1,1)d\nu]$. The rotational temperature can be derived as the following

$$T_R = 41.5 \text{ K} / \ln [1.06 \times \mathcal{C}(1,1) \times R^{12}] , \quad (1)$$

where $\mathcal{C}(1,1)$ is a numerical factor determined as

$$\mathcal{C}(1,1) = 0.003 + 2.26 \mathcal{R}^{sm} + 0.00032 e^{5.38 \mathcal{R}^{sm}} , \quad (2)$$

which is based on fitting the simulated NH_3 (1,1) spectra based on a grid of opacities and linewidth. The kinetic temperature is then (paper I)

$$T_k = 3.67 + 0.307 \times T_R + 0.0357 \times T_R^2 . \quad (3)$$

The full recipe is given in Kauffmann et al. (2012) and is generally applicable to a wide range of conditions in opacities, channel width, and intrinsic linewidth. In the observed linewidth range, the dependence of $\mathcal{C}(1,1)$ on linewidth is small. The uncertainty in derived kinetic temperature is then calculated using a Monte Carlo approach (paper I). For pixels with (2,2) detection, the representative 1σ uncertainty is about 1 to 2 K for emission peaks and between 2 K and 5 K for diffuse areas. Except for about 1.5% of scattered pixels, the derived temperatures are between 10 K and 30 K. When there is no detection of the (2,2) line, we derive an upper limit to kinetic temperatures (T_k^u) assuming $3\sigma(2,2)$ intensity. Figure 2 shows the derived temperatures overlaid with the dust continuum and dust cores. The temperatures generally drops while moving inward the dust cores, consistent with paper I at a coarser spatial grid. A quantitative analysis of the thermal structure of the whole region will be presented in Kauffmann et al. (2012).

The low velocity resolution of 0.62 km s^{-1} complicates the calculation of velocity dispersions. We first identify main group channels with signal-to-noise ratios > 3 . If more than one such channel is found, a dispersion σ_{data} is calculated, in which channels are weighted by their intensity; if a single channel is found, an upper dispersion limit of 0.26 km s^{-1} (channel

width) is adopted. The intrinsic dispersion of the (1,1) main group is then subtracted to obtain $\sigma_{\text{obs}} = [\sigma_{\text{data}}^2 - (0.2 \text{ km s}^{-1})^2]^{1/2}$. A numerical experiment was performed based on simulated Gaussian lines with noise. For our observed core-averaged SNR of 13 to 43 and typical dispersion of $<0.4 \text{ km s}^{-1}$, using only channels with $\text{SNR} > 3$ results in an underestimation of the intrinsic line dispersion by about 5%. This is negligible considering that we have used an upper limit for single channel detections.

To account for the internal centroid velocity variation, the standard deviation (σ_{pp}) among the peak velocities of spectra contained within each core was added to the pixel averaged velocity dispersion (σ_{obs}) as $\sigma_{\text{core}}^2 = \sigma_{\text{obs}}^2 + \sigma_{pp}^2$. The core velocity dispersion (σ_{core}) thus derived along with pixel-to-pixel velocity deviation are listed in Table 1.

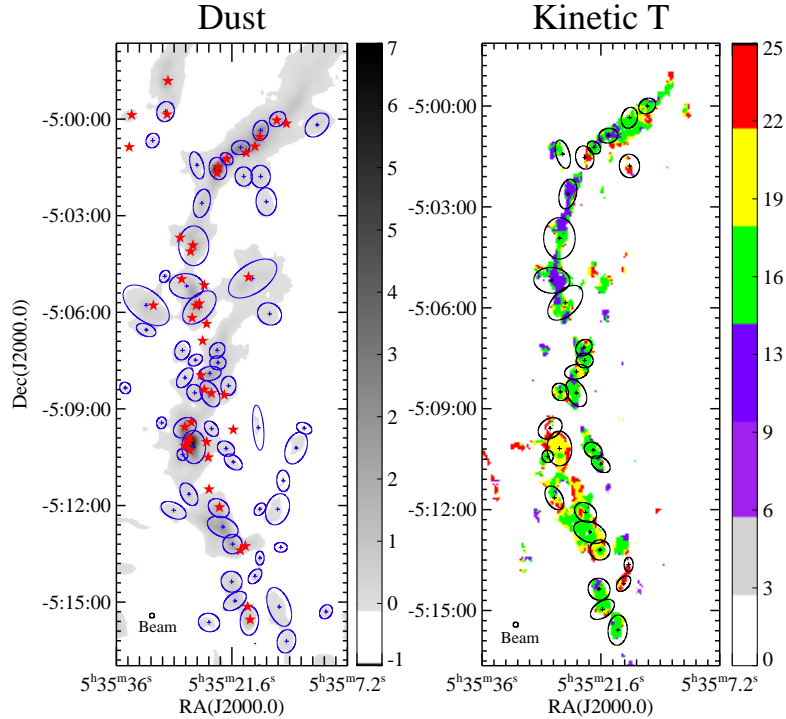


Fig. 2.— Left: $850 \mu\text{m}$ dust images with dust cores (N07). The red stars are embedded YSOs (Megeath et al. 2012) Right: Derived kinetic temperatures overlaid with cores.

4. Dynamic State of Cores

For a full coverage of all OMC2 and OMC3 cores, we use the SCUBA survey of Orion by Nutter & Ward-Thompson (2007, hereafter N07), who identified cores as ellipses in the signal to noise ratio map. They stated that the flux calibration is accurate to the level of about 10%. The uncertainty in the determination of dust mass comes mainly from the assumption of dust opacity, which is 45% lower in N07 than in Ossenkopf & Henning (1994). This should be kept in mind as a generic uncertainty in derived dust masses. We used the published dust mass in N07 and implement the following correction based on temperatures derived in this paper.

We select SCUBA cores with more than 50% of the pixels having a measured T_k based on NH_3 . These temperature measurements are weighted by dust column density and then averaged to be the core temperature T_{core} . A uniform dust temperature of 20 K was assume in N07. In our map, 74% of the pixels have derived temperature lower than 20 K. We therefore scale the core mass by the factor $B_{850,20\text{ K}}/B_{850,T_{core}}$, where $B_{850,T}$ is the Planck function at 850 μm and temperature T . The resulting core mass is generally larger than what is reported in N07. The derived core temperatures and core velocity dispersion are reported in Table 1.

We identify cores with and without embedded stars based on Spitzer source identifications (Figure 2). A core is deemed protostellar if the distance between its peak position and a YSO are less than the semi-minor axis of the core ellipse (Fig. 2 and Table 1).

4.1. Are Cores Gravitationally Bound?

McKee & Zweibel (1992) derive the virial theorem in Eulerian form to express explicitly the contribution of turbulent pressure both inside and surrounding the cloud

$$2c_w(\mathcal{E} - \mathcal{E}_0) + \mathcal{M}_s + \mathcal{G} = 0 , \quad (4)$$

where

$$c_w = 1 + \frac{\mathcal{E}_w - \mathcal{E}_{0w}}{2(\mathcal{E} - \mathcal{E}_0)} \quad (5)$$

is determined by the ratio of the difference between surface turbulent energy \mathcal{E}_{0w} and internal turbulent energy \mathcal{E}_w , and total surface kinetic energy \mathcal{E}_0 and total internal kinetic energy $\mathcal{E} = \frac{3}{2}M\sigma^2$. For a cloud with primarily turbulent motions, $c_w = 3/2$. If steady motions, such as rotation, are significant, c_w is close to unity. The velocity resolution of our data limits our ability to evaluate directly the role of turbulence, which could be dominant (McKee & Tan

2003). For a significant fraction of the pixels, we only have an upper limit to the linewidth, which results in an overestimation of the total core velocity dispersion. A unity c_w is thus assumed for simplicity for the virial mass calculation. \mathcal{M}_s is the magnetic energy associated with the cloud. \mathcal{G} is the gravitational potential energy. For an axisymmetric ellipsoid with concentric density profiles

$$\mathcal{G} = -\frac{3}{5}\alpha\beta\frac{GM^2}{r} , \quad (6)$$

where $\beta = \arcsin e/e$ is the geometry factor determined by eccentricity $e = \sqrt{1 - f^2}$ and $\alpha = (1 - a/3)/(1 - 2a/5)$ for a power law density profile $\rho \propto r^{-a}$. We adopt $a = 1.6$ for an isothermal cloud in equilibrium (Bonnor 1956). The intrinsic axis ratio f is smaller than the observed axis ratio f_{obs} due to projection. Myers et al. (1991) show that dark cloud cores are more likely to be prolate. Condensations in Orion are also statistically more consistent with being prolate rather than oblate (Li 2002). Based on the more general inversion from Fall & Frenk (1983), we derive an averaged true axis ratio \bar{f} corresponding to a sample of a single value, namely, the observed f_{obs} for a prolate ellipsoid

$$\bar{f} = \frac{2}{\pi}f_{obs}\mathcal{F}_1(0.5, 0.5, -0.5, 1.5, 1, 1 - f_{obs}^2) , \quad (7)$$

where \mathcal{F}_1 is the Appell hypergeometric function of the first kind, which gives $\bar{f} = 1$ for $f_{obs} = 1$ and $\bar{f} = 0$ for $f_{obs} = 0$. For values in between, we \bar{f} as a replacement of f in calculating the gravitational potential.

By assuming $\mathcal{M}_s = 0$ and $\mathcal{E}_0 = 0$, a simple virial mass can be derived using the virial theorem (Eq. 4)

$$M_{vir} = \frac{5}{\alpha\beta} \frac{\sigma^2 r}{G} . \quad (8)$$

The virial mass is the minimal mass for a cloud to be self-gravitating in the absence of pressure confinement and steady magnetic field. A "virial mass ratio" independent of B and \mathcal{E}_0 is defined as

$$R_{vir} = \frac{M}{M_{vir}} . \quad (9)$$

We find that 24 of 30 cores (Fig. 3 and Table 1), i.e., 80% have $R_{vir} > 1$, 11 cores (37%) fulfil $R_{vir} > 3$. The majority of the core sample are bound by gravity.

4.2. Stability and Critical Mass

The stability of cores are considered here in the context of external pressure and the internal magnetic field. The critical mass M_C is defined as the maximum mass which can

be stably supported by internal velocity dispersion and magnetic pressure. The two effects can be considered separately and then combined in a simple approximation

$$M_C = M_J + M_\Phi , \quad (10)$$

which is accurate to within 5% compared to the more rigorous calculations (McKee 1989).

The Jeans mass for a non-magnetic isothermal cloud (Bonnor 1956; McKee & Zweibel 1992) is

$$M_J = 1.182 \frac{c_w^{3/2}}{c_{pr}^{1/2}} \frac{\sigma^4}{G^{3/2} P_{ic}^{1/2}} , \quad (11)$$

where c_w parametrizes the pressure from turbulence outside of the cloud and c_{pr} parametrize the added internal pressure from turbulence’s disturbing B field. Jeans mass depends on the fourth power of the line width. If we consider tracers of more diffuse gas in this region, such as ^{13}CO , the linewidth is around 1.5 km s^{-1} (Melnick et al. 2011), definitely supersonic. We choose the combined factor to be in the middle of the possible range for turbulent gas $c_w^{3/2}/c_{pr}^{1/2} \sim 2.1$ (McKee & Zweibel 1992). The external pressure term can be estimated as

$$P_{ic} = n_{ic} \mu m_H \sigma_{ic}^2 , \quad (12)$$

where the mean molecular weight μ relative to $\text{n}(\text{H}_2)$ is 2.8 (Kauffman et al. 2008) and m_H is the proton mass. We take a lower bound value of 1 km s^{-1} FWHM for estimating σ_{ic} . The inter-cloud density n_{ic} is not well known. Radiative transfer analysis of CO, ^{13}CO , and H_2 in this region (Li 2002) show that the densities are a few times 10^4 cm^{-3} in the relatively diffuse area. We use a lower bound of 10^4 cm^{-3} to calculate the Jeans mass given in Table 1. The Jeans mass thus derived will be a conservative upper limit.

The maximum mass which can be supported by a steady B field alone is

$$M_\Phi = c_\Phi \frac{\pi B r^2}{G^{1/2}} , \quad (13)$$

where $c_\Phi \sim 0.12$ is given by numerical simulations (Mouschovias & Spitzer 1976; Tomisaka, Ikeuchi & Nakamura 1988).

Crutcher et al. (1999) detect the Zeeman effect in the CN 3mm line near Orion BN/KL. The field strength is derived to be 0.19 mG or 0.36 mG, based on different fitting schemes. This is larger than the $B \sim 0.03 \text{ mG}$ measured in dark clouds. Given the proximity of BN/KL to active star formation, the large B could be explained by rapid collapses’ freezing magnetic flux into high density regions along the line-of-sight. We thus take a smaller, nominal $B = 0.1 \text{ mG}$ for the quiescent Orion cores.

Using the critical mass calculated through Eq. 10, 11, and 13, we define the “critical mass ratio”

$$R_c = \frac{M}{M_c} . \quad (14)$$

We find that 12 out of 30 (40%) cores have $R_c > 1$.

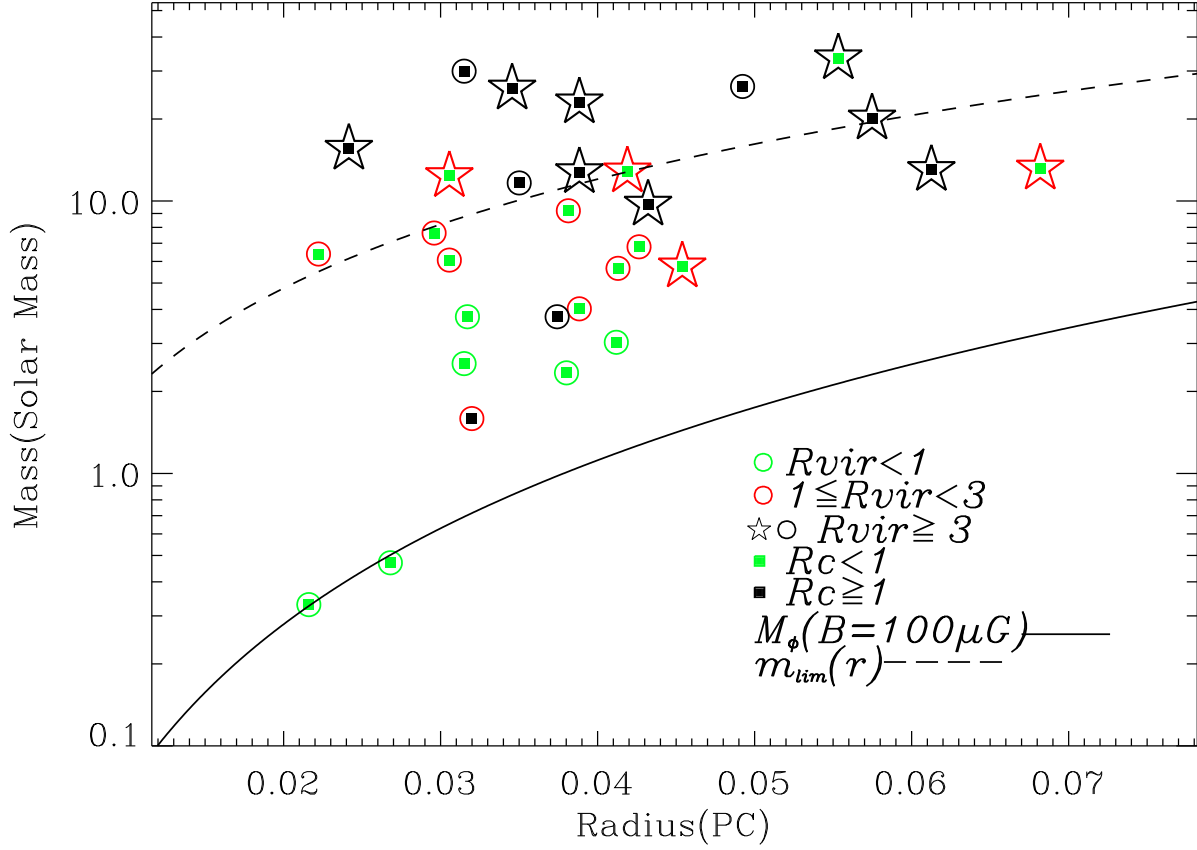


Fig. 3.— The core mass-size relationship similar to that in paper II. The colors of the open symbols denote the virial mass ratio R_{vir} , with green for $R_{vir} > 1$, red for $1 < R_{vir} < 3$ and black for $R_{vir} > 3$. Open stellar symbols are protostellar cores and open circles are starless cores. The colors of the solid squares denote the critical mass ratio R_c , with green for $R_c < 1$ and black for $R_c > 1$. The solid curve is for mass supported by a steady magnetic field of $100 \mu G$. The dashed curve represents the empirical threshold for massive star formation (Eq. 15).

4.3. Discussion: Is Orion Special?

Our data suggest mass ratios $R_{vir} > 3$ and $R_c > 1$ for most cores. This is different from other clouds in solar neighborhood within ~ 500 pc. In Perseus, Foster et al. (2008) and Kirk et al. (2007) find an equivalent $R_{vir} \lesssim 3$. In Ophiuchus, André et al. (2007) imply $R_{vir} \leq 1$ based on their Table 4 after adopting the dust opacity used here. For SCUBA-identified Gould Belt cores, Sadavoy et al. (2010) find that only 20 out of 354 cores have $M/M_J > 2$ (again adjusting dust opacities, and excluding their Orion data to avoid overlap). Their M_J represents a purely thermal Jeans mass, which means that these cores will have an even smaller mass ratio using our definitions.

The observed R_{vir} in Orion may be similar to those found in high mass star forming regions, e.g., the two clouds studied by Pillai et al. (2011). Although direct comparison is hard due to the much larger distance of other high star forming regions.

The calculations differ slightly between studies, e.g., in the factors α , β , and dust opacities. These differences alone cannot explain the larger mass ratios observed in Orion. Thus, our result that 60% of Orion cores have $R_{vir} > 3$ and 40% are supercritical is significant.

In many pixels, the NH_3 lines are not well resolved with a FWHM channel width of 0.62 km s^{-1} . For these pixels, the channel width was used as the upper limit of the intrinsic line width. Based on the combination of the measured line width and line width upper limits, the velocity dispersion of Orion cores do not exceed those of the cores in other regions studied by Kirk et al. (2007), André et al. (2007), and Foster et al. (2008). The higher values of R_{vir} and R_c of Orion cores are thus not due to different velocity field, but higher masses. Kauffmann & Pillai (2010) suggest that Ophiuchus and Perseus dense cores have a size-dependent limit

$$m_{\text{lim}}(r) = 870 M_{\odot} (r/\text{pc})^{1.33}, \quad (15)$$

above which high-mass star formation occurs. We find 12 cores (40%) above this threshold. Within the solar neighborhood, Orion cores seem to be the most likely ones to form high-mass stars.

5. Conclusions

We have mapped OMC2 and OMC3 in NH_3 (1,1) and (2,2) with both VLA and GBT. The combined single dish plus interferometric data provide a rare detailed look into the thermal and dynamic properties of a collection of massive quiescent cores. Our main results are:

1. We obtain good temperature measurement for 30 dust cores. The median core temperature is 17 K. The typical uncertainty for derived temperature of each pixel is about 2 K.
2. 12 cores are associated with a protostar. The average temperatures of the protostellar and the starless cores are similar suggesting that the heating in OMC2-3 region is primarily external.
3. A total of 24 cores (80%) are gravitationally bound ($R_{vir} > 1$), and 11 cores (37%) achieve $R_{vir} > 3$. Compared to other Gould Belt clouds, a much higher fraction of cores are tightly bounded.
4. 12 out of 30 cores (40%) are more massive than the critical mass defined as the combination of Jeans mass and mass supported by a steady magnetic field of 100 μG .

In summary, this sample of Orion cores, identified in dust emission with temperature and turbulence measured in NH_3 inversion lines, are proven to be well bounded by gravity and contains a substantial fraction of supercritical cores. They will evolve rapidly, either collapsing to form a star or fragmenting.

REFERENCES

- André, P., Belloche, A., Motte, F., & Peretto, N. 2007, *A&A*, 472, 519
- Benson, P. J. & Myers, P. C. 1989, *ApJS*, 71, 89
- Bonnor, W. B. 1956, *MNRAS*, 116, 351
- Chini, R., Reipurth, B., Ward-Thompson, D., et al. 1997, *ApJ*, 474, L135
- Crutcher, R. M., Troland, T. H., Lazareff, B., Paubert, G., & Kazès, I. 1999, *ApJ*, 514, L121
- Foster, J. B., Rosolowsky, E. W., Kauffmann, J., et al. 2009, *ApJ*, 696, 298
- Ho, P. T. P. & Townes, C. H. 1983, *ARA&A*, 21, 239
- Ikeda, N., Sunada, K., & Kitamura, Y. 2007, *ApJ*, 665, 1194
- Kauffmann et al. 2012, in prep.
- Kauffmann, J., Bertoldi, F., Bourke, T. L., Evans, N. J., II, & Lee, C. W. 2008, *A&A*, 487, 993

- Kauffmann, J., & Pillai, T. 2010, *ApJ*, 723, L7
- Kirk, H., Johnstone, D., & Tafalla, M. 2007, *ApJ*, 668, 1042
- Könyves, V., André, P., Men'shchikov, A., et al. 2010, *A&A*, 518, L106
- Li, D. 2002, Ph.D. Thesis,
- Li, D., Goldsmith, P. F., & Menten, K. 2003, *ApJ*, 587, 262 (Paper I)
- Li, D., Velusamy, T., Goldsmith, P. F., & Langer, W. D. 2007, *ApJ*, 655, 351 (Paper II)
- McKee, C. F. 1989, *ApJ*, 345, 782
- McKee, C. F., & Tan, J. C. 2003, *ApJ*, 585, 850
- McKee, C. F. & Zweibel, E. G. 1992, *ApJ*, 399, 551
- Megeath, S. T., Gutermuth, R., Muzerolle, J., et al. 2012, *AJ*, 144, 192
- Mookerjee, B., Kramer, C., Nielbock, M., & Nyman, L.-Å. 2004, *A&A*, 426, 119
- Mouschovias, T. C. & Spitzer, L. 1976, *ApJ*, 210, 326
- Myers, P. C., Fuller, G. A., Goodman, A. A., & Benson, P. J. 1991, *ApJ*, 376, 561
- Ossenkopf, V. & Henning, T. 1994, *A&A*, 291, 943
- Pillai, T., Kauffmann, J., Wyrowski, F., et al. 2011, *A&A*, 530, A118
- Reid, M. A., & Wilson, C. D. 2005, *ApJ*, 625, 891
- Sadavoy, S. I., Di Francesco, J., Bontemps, S., et al. 2010, *ApJ*, 710, 1247
- Takahashi, S., Saito, M., Ohashi, N., et al. 2008, *ApJ*, 688, 344
- Tatematsu, K., Kandori, R., Umemoto, T., & Sekimoto, Y. 2008, *PASJ*, 60, 407
- Tomisaka, K., Ikeuchi, S., & Nakamura, T. 1988, *ApJ*, 335, 239
- Velusamy, T., Peng, R., Li, D., Goldsmith, P. F., & Langer, W. D. 2008, *ApJ*, 688, L87 (Paper III)
- Vogel, S. N., Wright, M. C. H., Plambeck, R. L., & Welch, W. J. 1984, *ApJ*, 283, 655
- Ward-Thompson, D., André, P., Crutcher, R., Johnstone, D., Onishi, T. & Wilson, C. 2007, *Protostars and Planets V*, 33

Williams, J. P., Plambeck, R. L., & Heyer, M. H. 2003, *ApJ*, 591, 1025

Wiseman, J. J. & Ho, P. T. P. 1998, *ApJ*, 502, 676

Zhang, Q., Ho, P. T. P., & Wright, M. C. H. 2000, *AJ*, 119, 1345

Table 1. Temperatures and Engergy State of Orion Cores

Source	RA (J2000)	DEC (J2000)	T_{core} K	D_{core}^a Arcsec	σ_{core}^b km s ⁻¹	Mass M _☉	M _J M _☉	M _Φ M _☉	R_{vir}	R_c	YSO RA (J2000)	YSO DEC (J2000)	Seperation ^c Arcsec
OriAN-535161-50000	5:35:16	-5:00:00	16.	14.	0.56	12.	49.6	0.6	2.	0.2	5:35:16	-5:00:00	2.7
OriAN-535182-50021	5:35:18	-5:00:20	16.	16.	0.48	26.	21.9	0.8	6.	1.	5:35:19	-5:00:36	12.1
OriAN-535182-50147	5:35:18	-5:01:46	21.	19.	0.41	3.	7.8	1.2	0.9	0.3	5:35:19	-5:01:11	51.9
OriAN-535183-51338	5:35:18	-5:13:37	31.	10.	0.28	0.3	0.7	0.3	0.7	0.3	5:35:19	-5:13:11	35.1
OriAN-535189-51412	5:35:18	-5:14:12	30.	13.	0.27	0.5	0.7	0.5	0.8	0.4	5:35:21	-5:13:11	55.4
OriAN-535196-51535	5:35:19	-5:15:35	15.	21.	0.47	6.	16.3	1.4	1.	0.3	5:35:19	-5:15:36	2.7
OriAN-535207-50053	5:35:20	-5:00:52	14.	15.	0.33	30.	3.5	0.7	18.	7.	5:35:19	-5:01:11	14.2
OriAN-535214-51458	5:35:21	-5:14:57	19.	18.	0.37	4.	5.5	1.0	2.	0.6	5:35:19	-5:15:00	26.1
OriAN-535216-51039	5:35:21	-5:10:38	16.	15.	0.27	2.	0.7	0.7	2.	1.	5:35:23	-5:10:47	47.1
OriAN-535217-51312	5:35:21	-5:13:11	24.	18.	0.52	9.	24.1	1.0	2.	0.4	5:35:21	-5:13:11	18.9
OriAN-535218-51422	5:35:21	-5:14:21	16.	20.	0.37	6.	5.4	1.2	2.	0.9	5:35:19	-5:15:00	55.3
OriAN-535224-50114	5:35:22	-5:01:14	19.	11.	0.28	16.	0.7	0.4	28.	15.	5:35:21	-5:01:11	0.1
OriAN-535225-51014	5:35:22	-5:10:14	15.	15.	0.50	2.	29.6	0.7	0.5	0.1	5:35:23	-5:10:47	36.6
OriAN-535229-51240	5:35:22	-5:12:39	17.	23.	0.53	26.	20.3	1.7	5.	1.	5:35:23	-5:11:59	37.4
OriAN-535234-51205	5:35:23	-5:12:04	17.	18.	0.36	13.	4.4	1.0	6.	2.	5:35:23	-5:11:59	2.4
OriAN-535235-50132	5:35:23	-5:01:32	27.	18.	0.46	23.	20.5	1.0	5.	1.	5:35:23	-5:01:11	3.3
OriAN-535235-50734	5:35:23	-5:07:33	16.	14.	0.40	8.	9.1	0.6	3.	0.8	5:35:26	-5:07:48	39.1
OriAN-535236-50711	5:35:23	-5:07:10	17.	14.	0.49	6.	17.3	0.6	2.	0.3	5:35:26	-5:06:36	32.4
OriAN-535245-50754	5:35:24	-5:07:54	15.	16.	0.42	12.	8.2	0.9	4.	1.	5:35:26	-5:07:48	16.8
OriAN-535245-50832	5:35:24	-5:08:31	18.	20.	0.40	10.	6.1	1.3	3.	1.	5:35:23	-5:08:23	3.3
OriAN-535255-50237	5:35:25	-5:02:36	15.	20.	0.42	7.	13.1	1.3	2.	0.5	5:35:23	-5:01:48	63.4
OriAN-535258-50551	5:35:25	-5:05:50	19.	29.	0.39	13.	6.0	2.6	3.	2.	5:35:26	-5:05:59	7.0
OriAN-535261-50126	5:35:26	-5:01:26	16.	18.	0.34	4.	0.7	1.0	5.	2.	5:35:23	-5:01:11	38.9
OriAN-535264-50830	5:35:26	-5:08:30	18.	15.	0.51	4.	31.4	0.7	0.7	0.1	5:35:26	-5:08:23	18.9
OriAN-535265-50356	5:35:26	-5:03:56	19.	32.	0.68	13.	37.6	3.2	1.	0.3	5:35:26	-5:04:12	1.7
OriAN-535265-51011	5:35:26	-5:10:10	23.	26.	0.61	34.	36.2	2.1	4.	0.9	5:35:26	-5:10:12	9.7
OriAN-535271-51139	5:35:27	-5:11:39	20.	18.	0.43	2.	14.3	1.0	0.6	0.2	5:35:23	-5:11:24	38.5
OriAN-535274-50511	5:35:27	-5:05:11	13.	27.	0.34	20.	3.0	2.3	7.	4.	5:35:28	-5:04:47	15.7
OriAN-535276-50935	5:35:27	-5:09:34	28.	20.	0.72	13.	88.2	1.2	1.	0.1	5:35:26	-5:09:35	1.5
OriAN-535279-51025	5:35:27	-5:10:25	17.	10.	0.50	6.	32.6	0.3	2.	0.2	5:35:26	-5:10:12	15.5

^a R_{core} indicates the geometric mean of the long and short core axes.

^b σ_{core} is derived by averaging all spectra contained in a core and then measuring the line dispersion .

^cThe angular distance between dust contium peaks and their respective closest YSOs.